

CrossMark
click for updatesCite this: *J. Mater. Chem. A*, 2016, 4, 5137

Oxygen vacancy formation characteristics in the bulk and across different surface terminations of $\text{La}_{(1-x)}\text{Sr}_x\text{Fe}_{(1-y)}\text{Co}_y\text{O}_{(3-\delta)}$ perovskite oxides for CO_2 conversion†

Debtanu Maiti,^a Yolanda A. Daza,^a Matthew M. Yung,^b John N. Kuhn^a
and Venkat R. Bhethanabotla^{*a}

Density functional theory (DFT) based investigation of two parameters of prime interest – oxygen vacancy and surface terminations along (100) and (110) planes – has been conducted for $\text{La}_{(1-x)}\text{Sr}_x\text{Fe}_{(1-y)}\text{Co}_y\text{O}_{(3-\delta)}$ perovskite oxides in view of their application towards thermochemical carbon dioxide conversion reactions. The bulk oxygen vacancy formation energies for these mixed perovskite oxides are found to increase with increasing lanthanum and iron contents in the 'A' site and 'B' site, respectively. Surface terminations along (100) and (110) crystal planes are studied to probe their stability and their capabilities to accommodate surface oxygen vacancies. Amongst the various terminations, the oxygen-rich (110) surface and strontium-rich (100) surface are the most stable, while transition metal-rich terminations along (100) revealed preference towards the production of oxygen vacancies. The carbon dioxide adsorption strength, a key descriptor for CO_2 conversion reactions, is found to increase on oxygen vacant surfaces thus establishing the importance of oxygen vacancies in CO_2 conversion reactions. Amongst all the surface terminations, the lanthanum-oxygen terminated surface exhibited the strongest CO_2 adsorption strength. The theoretical prediction of the oxygen vacancy trends and the stability of the samples were corroborated by the temperature-programmed reduction and oxidation reactions and *in situ* XRD crystallography.

Received 15th December 2015
Accepted 3rd March 2016

DOI: 10.1039/c5ta10284g

www.rsc.org/MaterialsA

1. Introduction

The environmental and energy scenario of the world has resulted in active research towards recycling carbon dioxide.^{1,2} Carbon capture, utilization and sequestration (CCUS), an advanced methodology in comparison to only carbon capture and sequestration (CCS), has garnered a lot of attention recently.³ In this pursuit, the chemical route to fix carbon dioxide to hydrocarbon fuels has been quite popular.² Among the different existing protocols, the solar thermochemical approach has been of prime focus due to the natural reasons of utilizing the vast abundance of solar power in the process.^{4–9} A recent analysis of the feasibility and the potential of various solar-to-fuel processes by Mallapragada *et al.* revealed the thermochemical route to be the most viable option as well.¹⁰ There are reports of successful thermochemical carbon dioxide

conversion using concentrated solar energy to account for the high temperature requirements of the process.^{6,9,11}

The thermochemical conversion of carbon dioxide works in a simple two-step process, wherein, the first step involves the creation of oxygen deficient metal oxides by heating the materials at high temperature under inert conditions. In the subsequent second step, carbon dioxide flown over these oxygen vacant reduced materials is dissociated to carbon monoxide and the metal oxides get replenished of their lost oxygen. The success of this cyclic operation between stoichiometric and oxygen deficient materials for the conversion of carbon dioxide is dependent on the stability of the materials at both the stoichiometric and oxygen deficient conditions at high temperatures. Water splitting for the generation of hydrogen by a similar thermochemical principle has been studied as well, wherein the water vapor is passed instead of carbon dioxide and thus obtaining hydrogen instead of carbon monoxide.⁹ The conceptual picture of thermochemical carbon dioxide conversion is shown in Fig. 1. Carbon dioxide conversion, in general, has been found limited by the high temperature requirement and the scarcity of materials that can suffice the requirements of the thermochemical CO_2 splitting to CO. This situation has led to the origin of a modified carbon dioxide conversion cycle,

^aUniversity of South Florida, Tampa, FL 33620, USA. E-mail: bhethana@usf.edu^bNational Renewable Energy Laboratory, Golden, CO 80401, USA† Electronic supplementary information (ESI) available: Bulk phase $\text{La}_{0.5}\text{Sr}_{0.5}\text{FeO}_3$ configurations; charge density plots for site specific oxygen vacancy formation; surface terminations along (110) crystal facets of $\text{La}_{(1-x)}\text{Sr}_x\text{FeO}_3$; surface oxygen vacancies of $\text{La}_{(1-x)}\text{Sr}_x\text{Fe}_{(1-y)}\text{Co}_y\text{O}_3$; surface relaxations during oxygen vacancy formation. See DOI: 10.1039/c5ta10284g

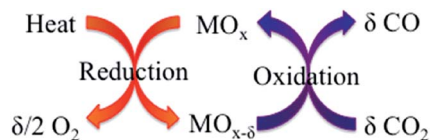


Fig. 1 General schematic of the thermochemical process.

wherein the reduction step is performed in the presence of hydrogen to produce more oxygen vacancies at lower temperatures. The second step of carbon monoxide production from carbon dioxide remains similar. This process of Reverse Water Gas Shift – Chemical Looping (RWGS-CL) has been found successful as studied by Daza *et al.*^{12,13} In general, the feasibility of the thermochemical and RWGS-CL processes is governed by the oxygen vacancy formation characteristics of the metal oxide. Amongst them, ceria, perovskite oxides and spinels are known to exhibit good oxygen vacancy characteristics. A pioneering work on thermochemical carbon dioxide conversion was reported using ceria.⁶ Subsequently, there were reports of success with the use of perovskite oxides and perovskite oxides on various supports.^{9,11,14} Perovskite oxides are a class of mixed metal oxides of the form ABO_3 , being used in applications like dielectrics, catalytic reactions, adsorbents, membranes, and solid oxide fuel cells.^{15–18} The thermal stability of these materials and stability under non-stoichiometric conditions are some of the few properties that make them so interesting.^{19,20}

Carbon dioxide conversion is strongly correlated to the extent of oxygen vacancy formation and the material's keenness to regain its lost oxygen. The reduction temperature of the material is thus an important parameter to look out for, as it represents the energy cost for oxygen vacancy formation and in the process perspective, it also reflects the cost of CO_2 conversion cycles. This property is closely related to the particular material composition. The oxygen vacancy characteristic is thus an intrinsic property of the material itself. Perovskite oxides provide a vast opportunity for tuning the material properties by substituting appropriate elements in their respective 'A' and 'B' sites of the ABO_3 type crystal structure. There have been reports of varying oxygen vacancy formations and lowering the reduction temperature *via* material composition tuning.^{13,21} The oxygen vacancy formation characteristics are probed experimentally as the extent of oxygen vacancy formation, the onset and peak temperature of vacancy formation and computationally as the energy of oxygen vacancy formation at different vacancy concentrations. A considerable amount of theoretical effort has been expended in recent years to obtain optimum candidates for the thermochemical conversion by calculating oxygen vacancy formation energy using density functional theory.^{22–24} Lanthanum based perovskite oxides have been found to work well for these processes.^{9,12,13,23} The effects of strontium substitution in the 'A' site and manganese and aluminum composition in the 'B' site have been reported by Deml *et al.*²³ Screening across a range of transition metals has also been performed to find the optimum perovskites to be used for this purpose.²⁴ Probing the energy of oxygen vacancy formation in the bulk is thus an important route for predicting the appropriate material for the carbon dioxide conversion processes. However,

the carbon dioxide adsorption, dissociation and desorption of CO occur only at the surface of the materials. Hence, a critical understanding of the surface structure, stability and reactions is important as well. These perovskite oxides can exhibit different surface terminations. It is thus relevant to know which surface terminations are more probable to be present in nature, which of them are more likely to accommodate oxygen vacancies under experimental conditions and most importantly which of them exhibit the ideal sites for CO_2 conversion reactions. With the recent knowledge of synthesis protocols for growth of preferred crystal facets and terminations in perovskites and double perovskites,^{25–28} prediction of the best sites on these perovskite materials towards CO_2 conversion materials becomes more pertinent.

This article is focused on the bulk oxygen formation characteristics and surface oxygen vacancy characteristics of $La_{(1-x)}Sr_xFe_{(1-y)}Co_yO_{(3-\delta)}$ with $x = 0.25$ or 0.5 and $y = 0$ or 0.5 or 1 . The most stable bulk crystal structures of $La_{0.5}Sr_{0.5}BO_3$ and $La_{0.75}Sr_{0.25}BO_3$ with $B = Co$ or Fe or $Fe_{0.5}Co_{0.5}$ are predicted. Along with the investigations on oxygen vacancy formation energies with varying 'A' site and 'B' site compositions, dependence of vacancy formation on the different sites of bulk materials has been reported as well. The theoretical trends are corroborated by the temperature-programmed reduction of the perovskites both in inert and hydrogen environments. The materials exhibited great stability under oxygen deficient conditions as predicted by theoretical trends. Although there have been several studies on the strontium segregation on perovskite type oxides based on XPS, XAS and LEIS studies and computational techniques,^{29–32} a rigorous analysis of the various terminations is absent. A detailed study is, hence, performed to probe the stability of the pure stoichiometric surface terminations along the $\langle 100 \rangle$ and $\langle 110 \rangle$ directions. Oxygen vacancy formation tendencies on these different terminations are henceforth examined to predict the surface terminations that are more likely to exhibit oxygen vacancies. Finally, the effect of these terminations, both under pure conditions and under oxygen deficient conditions, on carbon dioxide conversion has been studied by calculating the carbon dioxide adsorption strength on the different surface terminations along (100) crystal planes of $La_{0.5}Sr_{0.5}FeO_3$. The most potent surface terminations that can convert carbon dioxide are thus predicted. This is based on the concept of using suitable descriptors for probing reactions and finding desired materials for the same as had been reported in the literature.^{33–35} A recent work has also revealed the correlation of carbon dioxide conversion performance with carbon dioxide adsorption strengths.¹³ Overall, this study is an effort for better understanding of the material dependent oxygen evolution process and to highlight the importance of surface terminations for accurate prediction of oxygen vacancy formation under experimental conditions and carbon dioxide conversion on the preferred surfaces of these perovskite oxides.

2. Computational methods

Density functional theory (DFT) based calculations are performed using Vienna *ab initio* Simulation Package (VASP – 5.2.8).^{36–40} All the calculations used plane wave basis set and gradient

generalization for the approximation of the electron densities. The core electronic states are treated by projector augmented wave (PAW) potentials^{41,42} and Perdew Wang – 91(PW-91)⁴³ variant of exchange correlation. Default potentials for lanthanum, strontium, iron and cobalt are consistently used while soft potentials are used for oxygen. Throughout the study, a constant energy cut off of 500 eV has been used. The convergence criterion for the ionic relaxations is set at 0.001 eV per atom. All the bulk phase systems studied are cubic, with 5 atoms in a unit cell and 40 atoms in a $2 \times 2 \times 2$ supercell, while 80 atoms containing surface slabs are made of $2 \times 2 \times 4$ supercells with 15 Å of vacuum along the surface direction to mimic the absence of atomic periodicity on surfaces. Convergence with respect to the k point sampling has been checked; finally, calculations for all the 40 atom supercell of bulk stoichiometric and non-stoichiometric perovskites are performed with a $4 \times 4 \times 4$ k point mesh generated by an automatic scheme having Monkhorst Pack grid. Magnetic effects are not considered explicitly as it was known to have minor effects in the systematic trends of energy.²⁴ For the slab calculations of the surface structures, dipole correction has been accounted.⁴⁴

The initial ground state configurations for each of the materials are obtained through a series of varying cell volume calculations. Once the ground state lattice constant is established, the entire set of parameters is used for the nonstoichiometric calculations as well. Though oxygen vacancy formation in a material is a complex process consisting of several steps, the major energy intensive step is the dissociation of the metal–oxygen bond. Hence, computational oxygen vacancy formation energies calculated as the enthalpy difference between the initial stoichiometric material and the final oxygen deficient material along with gas phase oxygen mostly represent the energy barrier for the dissociation of the metal–oxygen bonds and the subsequent relaxation of the oxygen deficient structure. The creation of oxygen vacancies is marked by the systematic removal of oxygen atoms, either from bulk or the surface. The extent of oxygen vacancy (δ) is defined as the oxygen deficiency per unit molecule of ABO_3 ; thus in a 40 atom supercell of perovskites, $\delta = 0.125$ and 0.25 are marked by the removal of one oxygen atom and two oxygen atoms, respectively. For surface oxygen vacancies of $\delta = 0.125$ and 0.25 , the number of oxygen atoms removed from the 80 atom supercell was two and four, respectively. The oxygen vacancy formation energy is calculated as per eqn (1).

$$E_{\text{vac}} = E_{\text{ABO}_{3-\delta}} + \delta \times \frac{n}{2} E_{\text{O}_2} - E_{\text{ABO}_3} \quad (1)$$

where, E_{ABO_3} is the total energy of the pure stoichiometric perovskite supercell having n unit cells, while $E_{\text{ABO}_{3-\delta}}$ is that of the oxygen vacant perovskite supercell, ' n ' representing the number of unit cells considered (8 for bulk calculations and 16 for surface calculations) and E_{O_2} is the molecular energy of oxygen. All the oxygen vacancy formation energies (E_{vac}/n) are expressed as the energy to create ' δ amount of oxygen vacancy' per ABO_3 . The oxygen over-binding error has been addressed by Wang *et al.* for PBE functionals by using a correction factor of 1.36 eV.⁴⁵ The correction factor for PW-91 (O_2) functional has been calculated to be 0.33 eV by Lee *et al.*⁴⁶ All the calculations of

oxygen vacancy formation energy has been corrected by this factor. The oxygen vacancy formation energies were also calculated using DFT + U to account for the Hubbard U correction for the transition metals on the B sites. The carbon dioxide adsorption energy on the materials is reported based on eqn (2).

$$E_{\text{ads}} = E_{\text{P+CO}_2} - E_{\text{CO}_2} - E_{\text{P}} \quad (2)$$

where, E_{P} is the energy of either pure or oxygen vacant perovskite, $E_{\text{P+CO}_2}$ is the energy of the combined system of CO_2 adsorbed on the perovskite, while E_{CO_2} is the energy of molecular gaseous CO_2 .

Charge density analysis was performed to probe the surface terminations and the various oxygen removal sites. The charge associated with an atom has been calculated using the Bader charge analysis code by Henkelman *et al.*^{47–49} The charge density plots were carried out using VESTA.⁵⁰

3. Experimental methodology

The $\text{La}_{0.75}\text{Sr}_{0.25}\text{Fe}_{(1-y)}\text{Co}_y\text{O}_3$ ($y = 0, 0.5$ and 1) samples were synthesized by the Pechini method, as described previously.¹² The oxygen vacancy formation under inert (He) and hydrogen (10% H_2/He) was measured by temperature-programmed oxygen vacancy formation (TPOvac) and temperature-programmed reduction (TPR), respectively, from room temperature to 950 °C. All experimental elements are described elsewhere in detail.⁵¹ The final calcination (synthesis) temperature of the samples used in the TPOvac and TPR experiments was 750 °C (ref. 12) and 950 °C (ref. 13), respectively. The stability of the crystal structure of the $\text{La}_{0.75}\text{Sr}_{0.25}\text{CoO}_3$ (calcined at 750 °C) oxide while heating under an inert atmosphere was tested *via in situ* X-ray diffraction using a Bruker D8 X-ray diffractometer with $\text{Cu K}\alpha$ ($\lambda = 0.154 \text{ nm}$) _{α} at a heating rate of 25 °C min^{-1} . The experimental elements of the *in situ* XRD can also be found elsewhere in more detail.¹²

Three RWGS-CL experiments were performed on the $\text{La}_{0.75}\text{Sr}_{0.25}\text{FeO}_3$ (calcined at 950 °C). In these experiments, the sample was heated in He to 550 °C and was reduced for 3, 13 or 17 min in 10% H_2/He . After 20 min of He flow, CO_2 was introduced (10% CO_2/He) until CO was no longer produced. Further experimental details can be found elsewhere.¹³ The results for the amount of H_2O produced during H_2 -reduction and CO produced during CO_2 flow are quantified in Fig. 12.

4. Results and discussion

4.1. Bulk crystal structure

$\text{La}_{0.75}\text{Sr}_{0.25}\text{Fe}_{(1-y)}\text{Co}_y\text{O}_3$ ($y = 0, 0.5$ and 1) and $\text{La}_{0.5}\text{Sr}_{0.5}\text{CoO}_3$ samples, as prepared by the Pechini method, revealed the presence of mixed crystalline phases with a predominance of the cubic phase. Although the diffraction pattern revealed the general crystallographic structures, it was unable to provide the details of the elemental organization within the structure itself. The local distribution of the ions is expected to have effects on the electronic and charge distribution within the material. Hence, a systematic study over a set of plausible bulk phase

configurations has been conducted *via* theoretical calculations. Only the cubic phase has been the focus of this study as the cubic phase was found prevalent experimentally. Furthermore, the different crystalline phases of perovskite oxides like orthorhombic, tetragonal and hexagonal tend to shift to high symmetry configurations like the cubic phase at high temperatures.^{52,53} Since the thermochemical reaction temperatures are also high enough ($\sim 1000^\circ\text{C}$ and above), it is quite justified to accept the cubic phase as the system of study. Moreover, the trends of oxygen vacancy formation were found invariant to the bulk phase structure of the material.²⁴ Within these high symmetry cubic phases (space group $Pm\bar{3}m$), the lattice organization of the individual 'A' and 'B' site elements led to the generation of several configurations. Fig. S1† shows a few possible bulk phase cubic configurations of $\text{La}_{0.5}\text{Sr}_{0.5}\text{FeO}_3$, made through a random distribution of lanthanum and strontium atoms in a supercell of 40 atoms having 4 atoms of lanthanum, 4 atoms of strontium, 8 atoms of iron and 24 atoms of oxygen. The configuration having the least energy, as calculated by density functional theory, was chosen to be the most stable one. The stable configurations of all the six samples (various La : Sr and Co : Fe ratios) are shown in Fig. 2. The stable configurations of $\text{La}_{0.5}\text{Sr}_{0.5}\text{BO}_3$ (B=Fe or Co or $\text{Fe}_{0.5}\text{Co}_{0.5}$) revealed the preference for alternate layering of lanthanum and strontium atoms (as shown in configuration (a) in Fig. S1† and 2a–c) while, all the stable configurations of $\text{La}_{0.75}\text{Sr}_{0.25}\text{BO}_3$ (B=Fe or Co or $\text{Fe}_{0.5}\text{Co}_{0.5}$) showed tendency to form linear chains of strontium surrounded by lanthanum layers as shown in Fig. 2d–f. A gradual increase of cell volume with the replacement of cobalt with iron on the 'B' site is evident from the increase in lattice constants (Table 1).

4.2. Bulk oxygen vacancies

A crucial factor that governs the carbon dioxide reduction in thermochemical cycles is the extent of oxygen vacancies. Oxygen

Table 1 Lattice constants of $\text{La}_{(1-x)}\text{Sr}_x\text{Fe}_{(1-y)}\text{Co}_y\text{O}_{(3-\delta)}$

Material	a (Å)	Material	a (Å)
$\text{La}_{0.5}\text{Sr}_{0.5}\text{CoO}_3$	3.835	$\text{La}_{0.75}\text{Sr}_{0.25}\text{CoO}_3$	3.835
$\text{La}_{0.5}\text{Sr}_{0.5}\text{Fe}_{0.5}\text{Co}_{0.5}\text{O}_3$	3.8435	$\text{La}_{0.75}\text{Sr}_{0.25}\text{Fe}_{0.5}\text{Co}_{0.5}\text{O}_3$	3.8535
$\text{La}_{0.5}\text{Sr}_{0.5}\text{FeO}_3$	3.857	$\text{La}_{0.75}\text{Sr}_{0.25}\text{FeO}_3$	3.8695

vacancy formation energy provides insights into the ease of oxygen removal and oxygen refilling. The trends of the oxygen vacancy formation energy for the bulk system of $\text{La}_{(1-x)}\text{Sr}_x\text{Fe}_{(1-y)}\text{Co}_y\text{O}_3$ for different extents of oxygen vacancies ($\delta = 0.125, 0.25$ and 0.375) are portrayed in Fig. 3a. A systematic trend was observed for the composition dependent oxygen vacancy generation. It was found easier with increasing strontium in the 'A' site and decreasing iron content in the 'B' site as revealed in Fig. 3b; this trend is in support of earlier reports as well.²³ This aspect is also corroborated experimentally for the $\text{La}_{0.75}\text{Sr}_{0.25}\text{Fe}_{(1-y)}\text{Co}_y\text{O}_3$ samples as shown in Fig. 4a. For both the TPOvac and TPR experiments, iron-rich materials exhibit lower oxygen vacancy formation, that too at higher peak temperatures, thus indicating a higher energy barrier for oxygen vacancy generation. The quantification of the $\text{H}_2\text{O}/\text{ABO}_3$ produced during TPR experiments was performed from room temperature to 600°C . The trend of oxygen vacancy formation energies with varying B sites is revealed in Fig. S2,† when the calculations were performed using DFT + U, with U values of 2, 3 and 4 for the B site elements.

Formation of higher extents of oxygen vacancy is expected to have higher energy requirements (as revealed in Fig. 3a), but the exciting aspect being revealed was that the energy cost scales almost linearly with the extent of oxygen vacancy (Fig. 3a). This result suggested a significant stability of the materials under high oxygen vacant conditions. Being stable at higher oxygen

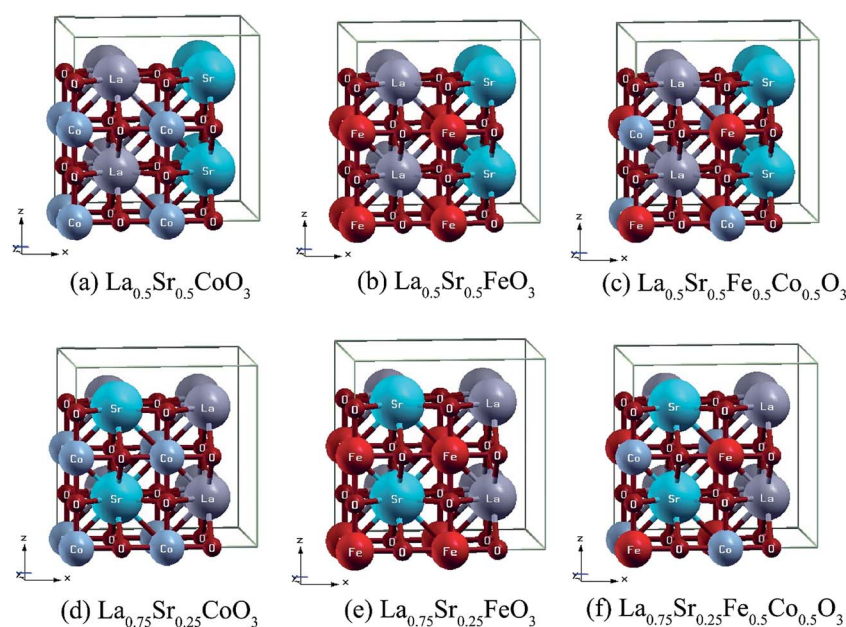


Fig. 2 Most stable bulk phase configurations of $\text{La}_{(1-x)}\text{Sr}_x\text{Fe}_{(1-y)}\text{Co}_y\text{O}_{(3-\delta)}$.

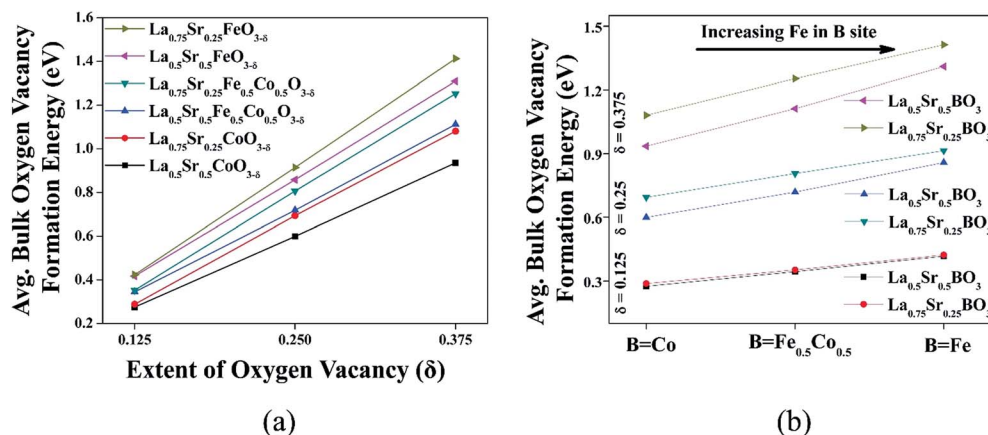


Fig. 3 Bulk oxygen vacancy trends in $\text{La}_{1-x}\text{Sr}_x\text{Fe}_{1-y}\text{Co}_y\text{O}_{3-\delta}$ for $\delta = 0.125, 0.25$ and 0.375 .

vacancies and not decomposing to other compounds is an essential requirement for the successful operation of this carbon dioxide conversion process. This aspect is also corroborated in Fig. 4b for the $\text{La}_{0.75}\text{Sr}_{0.25}\text{CoO}_3$ sample. Monitoring the crystalline structure evolution during the formation of oxygen vacancies (Fig. 4b) demonstrated the stability of the cubic crystalline structure. The XRD lines shifted to lower $2\theta^\circ$ as the temperature is increased, due to the expansion of the lattice. The lowest $2\theta^\circ$ values are achieved at the peak O_2 evolution temperature. As the sample cools, it returns to its original state, upon re-oxidation of the structure.

A systematic study of the site specific oxygen vacancy formation was also conducted. Studies of oxygen mobility or transport are dependent on cation ordering and thus on the site specificity of oxygen vacancy generation as well.^{54,55} Table 2 lists the site specific oxygen vacancy energies for $\text{La}_{0.5}\text{Sr}_{0.5}\text{BO}_3$.

For all the different extents of oxygen vacancies, oxygen removal from the lanthanum layer was much favorable to that from a strontium layer. An oxygen atom being removed from a lanthanum layer and a strontium layer involves breaking the electronic interactions of the oxygen atom with the neighboring 'A' site and 'B' site atoms. Removal of a neutral oxygen atom from a B–O bond leaves the electron cloud of B free to redistribute across the nearby atoms. Thus, not only the B site elements change their oxidation states, but also the nearby oxygen atoms and 'A' site elements obtain a share of the electron cloud by the inductive effect. While the presence of d orbitals in lanthanum can make it easier to accommodate the electrons, its smaller ionic radius makes it also exhibit a lesser screening effect than strontium and hence allows for a better charge flow across the lattice. Charge analysis based on Bader's method revealed a much stronger effect on the nearby B site atoms when a vacancy is generated in the strontium layer. Charge transfer was found much easier in the lanthanum layer. Hence, when a vacancy is formed in the lanthanum layer, the electron cloud gets re-distributed across the lanthanum layer easily. While in the strontium layer, the charge transfer was not favorable in the strontium layer itself resulting in higher charge accumulation on the B site atoms which further affects the neighboring lanthanum layer. This energy cost of electron

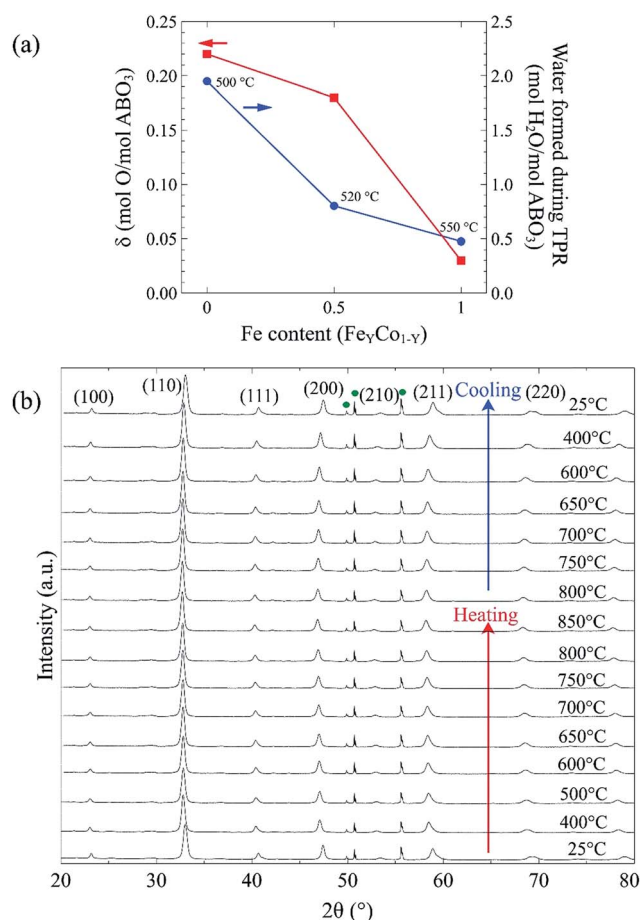


Fig. 4 (a) Ratio of oxygen removal from the $\text{La}_{0.75}\text{Sr}_{0.25}\text{Fe}_{1-y}\text{Co}_y\text{O}_3$ ($y = 0, 0.5$ and 1) samples under inert environment (left) and under 10% H_2/He (right). In the TPR experiments, the H_2O removed was quantified up to 600 $^\circ\text{C}$, and the numbers represent the peak reduction temperature for the quantified area. (b) *In situ* XRD of the cubic $\text{La}_{0.75}\text{Sr}_{0.25}\text{CoO}_3$ ($x = 0.25, y = 1$) under 50 sccm of He. The sample was heated from room temperature to 850 $^\circ\text{C}$ at 25 $^\circ\text{C min}^{-1}$ and cooled back to room temperature. The diffraction lines at 50, 51 and 55 $2\theta^\circ$ are due to the quartz sample holder.

Table 2 Site specificity of bulk oxygen vacancy formation energy

Material name	Extent of oxygen vacancy (δ)	Oxygen vacancy formation energy (eV)	
		in La Layer	in Sr Layer
$\text{La}_{0.5}\text{Sr}_{0.5}\text{CoO}_3$	0.125	0.2483	0.3191
	0.25	0.5553	0.6680
	0.375	0.8712	1.0053
$\text{La}_{0.5}\text{Sr}_{0.5}\text{Fe}_{0.5}\text{Co}_{0.5}\text{O}_3$	0.125	0.3255	0.3845
	0.25	0.6687	0.7902
	0.375	1.0375	1.1908
$\text{La}_{0.5}\text{Sr}_{0.5}\text{FeO}_3$	0.125	0.3992	0.4506
	0.25	0.8276	0.9256
	0.375	1.2299	1.3805

re-distribution in the strontium layer makes it harder for oxygen vacancy creation in that layer. The charge density difference plots between the pure and oxygen vacant structures for $\text{La}_{0.5}\text{Sr}_{0.5}\text{FeO}_3$ and $\text{La}_{0.5}\text{Sr}_{0.5}\text{CoO}_3$ are shown in Fig. 5a–d. Studies on double perovskites have shown the effect of cation ordering and site preference towards oxygen vacancy formation.^{54,56}

Apart from these, we could also find that a series of oxygen vacancies, producing a ‘vacancy tunnel’ like structure, was more

favorable than a random distribution of oxygen vacancies throughout the material. There have been reports of similar stable row vacancies in a brownmillerite type of structure.^{57–59} For both the lanthanum-rich layer and strontium-rich layer of $\text{La}_{0.5}\text{Sr}_{0.5}\text{FeO}_3$, randomly distributed oxygen vacancy formation was found to have ~ 0.06 eV higher energy barrier than that for continuous vacancy tunnel formation. Oxygen vacancies along a row of ‘B–O’ axis and concentrated vacancies around B site metals are also favored. Fig. S3† reveals the energy of vacancy tunnel formation and random vacancy creation in the bulk $\text{La}_{0.5}\text{Sr}_{0.5}\text{FeO}_3$ material along with their respective charge density difference plots. Other materials like $\text{La}_{0.5}\text{Sr}_{0.5}\text{CoO}_3$ and $\text{La}_{0.5}\text{Sr}_{0.5}\text{Fe}_{0.5}\text{Co}_{0.5}\text{O}_3$ also exhibit similar trends.

4.3. Surface structure

The different crystal facets present in $\text{La}_{(1-x)}\text{Sr}_x\text{Fe}_{(1-y)}\text{Co}_y\text{O}_3$ were revealed in the XRD study.¹³ The two major crystallographic planes prevalent were (100) and (110). Mixed perovskite oxides of this nature behold the possibility of exhibiting various surface terminations along these planes, based on the elemental presence on those surface terminations. Probing the different surface terminations and their role towards the thermochemical reactions of interest was hence important. For the

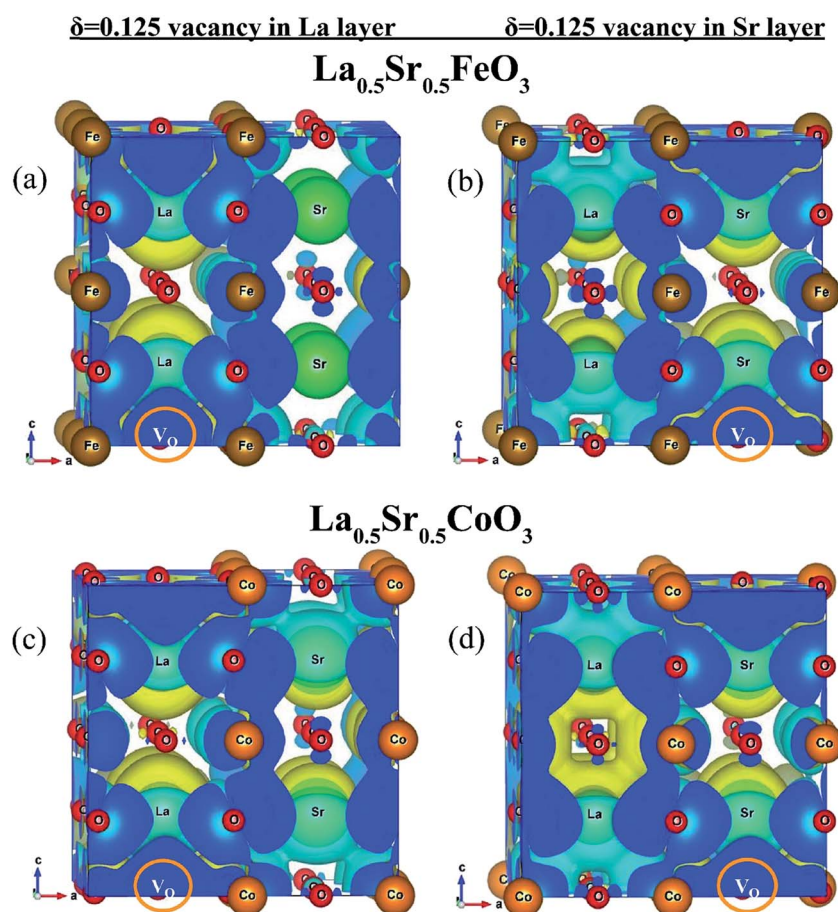


Fig. 5 Charge density difference maps for the oxygen removal from lanthanum-rich and strontium layers of (a and b) $\text{La}_{0.5}\text{Sr}_{0.5}\text{FeO}_3$ and (c and d) $\text{La}_{0.5}\text{Sr}_{0.5}\text{CoO}_3$.

materials of focus, $\text{La}_{(1-x)}\text{Sr}_x\text{Fe}_{(1-y)}\text{Co}_y\text{O}_3$, six different terminations were found to exist along the (100) facets of both $\text{La}_{0.5}\text{Sr}_{0.5}\text{BO}_3$ and $\text{La}_{0.75}\text{Sr}_{0.25}\text{BO}_3$ where 'B' stands for the different 'B' site components like Fe or Co or $\text{Fe}_{0.5}\text{Co}_{0.5}$. These six surface terminations were broadly classified into two major groups: 'AO' terminations (surfaces having an atomic layer of 'A' site metal and oxygen on the surface) and 'BO' terminations (surfaces having an atomic layer of 'B' site metal and oxygen on the surface). Each of these two classes has three variations based on the A site composition on the surface or in the

immediate sub-surface. For the 'AO' surface terminations of $\text{La}_{0.5}\text{Sr}_{0.5}\text{BO}_3$, the three variations of 'A' composition were (i) only lanthanum, (ii) lanthanum and strontium with 1 : 1 ratio (or $\text{La}_{0.5}\text{Sr}_{0.5}$) and (iii) only strontium. Similarly, the 'AO' compositions for $\text{La}_{0.75}\text{Sr}_{0.25}\text{BO}_3$ were (i) only lanthanum (ii) lanthanum and strontium in a ratio of 3 : 1 (or $\text{La}_{0.75}\text{Sr}_{0.25}$) and (iii) lanthanum and strontium with 1 : 1 ratio (or $\text{La}_{0.5}\text{Sr}_{0.5}$).

The different 'BO' surfaces were classified based on the different 'AO' compositions that lie in the immediate sub-surface. The nomenclature of the 'AO' surfaces was thus made

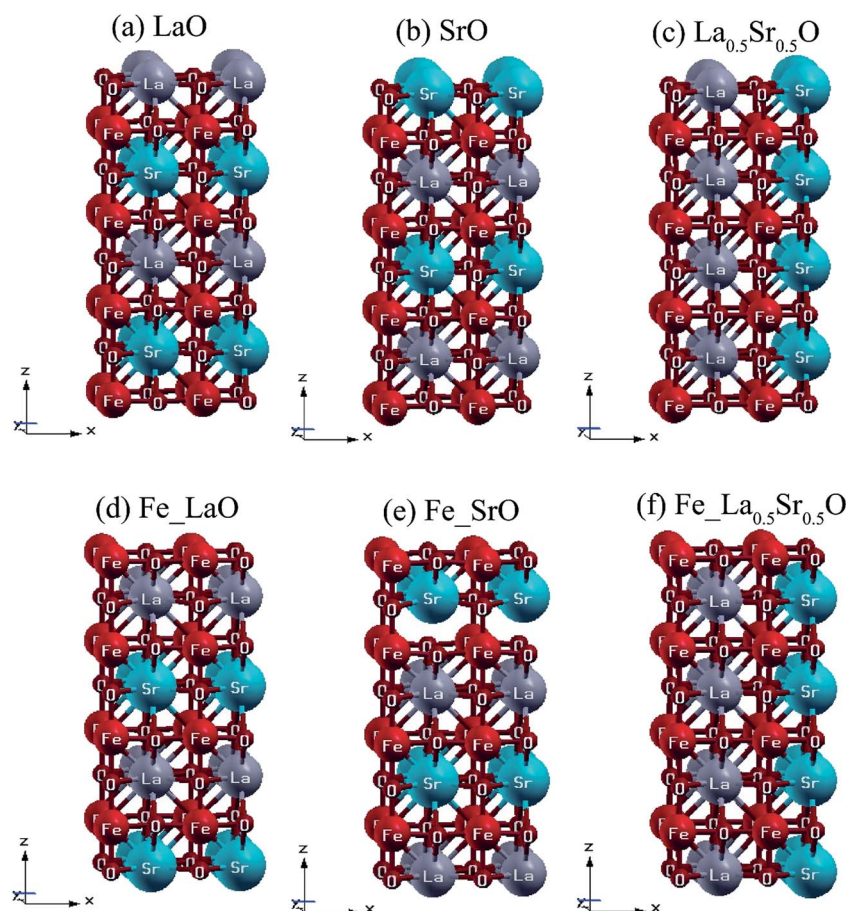


Fig. 6 (a–f) Various surface terminations along (100) facets of $\text{La}_{0.5}\text{Sr}_{0.5}\text{FeO}_3$.

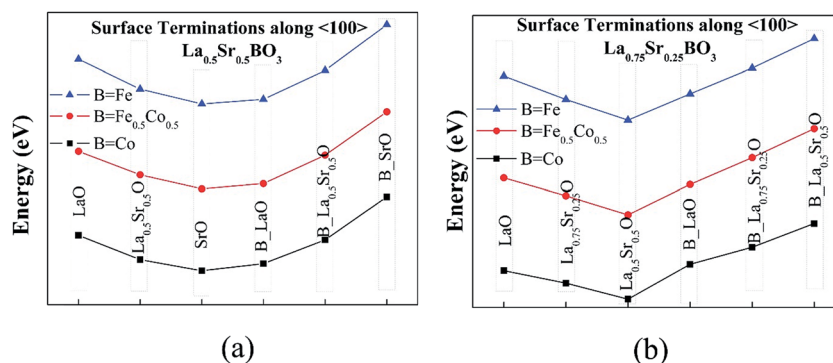


Fig. 7 Stability of the surface terminations along (100) crystal planes for (a) $\text{La}_{0.5}\text{Sr}_{0.5}\text{BO}_3$ and (b) $\text{La}_{0.75}\text{Sr}_{0.25}\text{BO}_3$ [B = Co, $\text{Fe}_{0.5}\text{Co}_{0.5}$ and Fe].

Table 3 Relaxation in the top layer of a few (100) surface terminations of $\text{La}_{0.5}\text{Sr}_{0.5}\text{FeO}_3$

Relaxation in the top most layer	(100) surface terminations of $\text{La}_{0.5}\text{Sr}_{0.5}\text{FeO}_3$			
	LaO	SrO	Fe_LaO	Fe_SrO
Absolute value (pm)	5.366	9.679	6.255	10.252
% of the bulk interlayer distance	2.82	4.96	3.28	5.25

according to the initials of the composition and that for 'BO' surfaces was done as per the B-atop-AO-sub-layer or in short B_AO. The representative structures for these six surface terminations along (100) cubic facets of $\text{La}_{0.5}\text{Sr}_{0.5}\text{FeO}_3$ are shown in Fig. 6a–f.

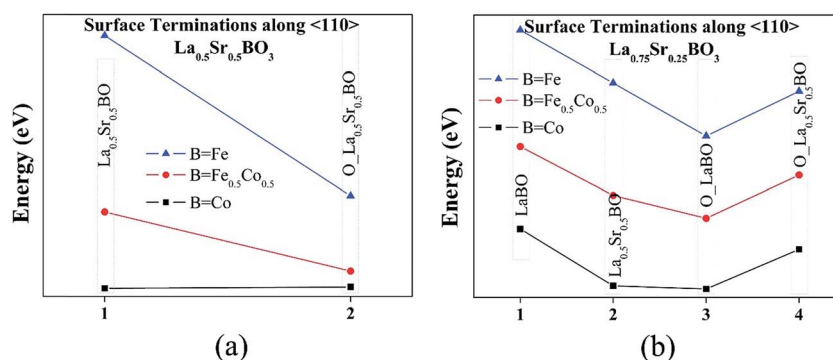
Theoretical studies on the stability of these surfaces are shown in Fig. 7a and b. A trend of stability was seen amongst the six different surface terminations along (100) surfaces of $\text{La}_{0.5}\text{Sr}_{0.5}\text{BO}_3$ and $\text{La}_{0.75}\text{Sr}_{0.25}\text{BO}_3$. For the 'AO' terminations, a higher content of strontium exposed to the surface was preferred in comparison to lanthanum. The orders of stability for 'AO' terminations in $\text{La}_{0.5}\text{Sr}_{0.5}\text{BO}_3$ and $\text{La}_{0.75}\text{Sr}_{0.25}\text{BO}_3$ materials are thus: $\text{SrO} > \text{La}_{0.5}\text{Sr}_{0.5}\text{O} > \text{LaO}$ and $\text{La}_{0.5}\text{Sr}_{0.5}\text{O} > \text{La}_{0.75}\text{Sr}_{0.25}\text{O} > \text{LaO}$, respectively. This result is in accordance with several studies that demonstrate strontium segregation to the surface.^{30,32,60} Experimental investigation by Druce *et al.* supports this result, although it relates this feature not only to simple surface relaxation, but also an extensive surface reconstruction.³² On the other hand, the stability of the 'BO' terminations is related to the composition of the 'AO' layer in the sub-surface. Increasing the strontium content in the immediate sub surface tends to destabilize the 'BO' surface termination. Hence, the orders of stability for 'BO' termination for $\text{La}_{0.5}\text{Sr}_{0.5}\text{BO}_3$ and $\text{La}_{0.75}\text{Sr}_{0.25}\text{BO}_3$ materials are as: $\text{B_LaO} > \text{B_La}_{0.5}\text{Sr}_{0.5}\text{O} > \text{B_SrO}$ and $\text{B_LaO} > \text{B_La}_{0.75}\text{Sr}_{0.25}\text{O} > \text{B_La}_{0.5}\text{Sr}_{0.5}\text{O}$, respectively. Amongst all the six surface terminations, the 'AO' termination having the highest strontium content proved to be the most stable. This stability pattern was valid for all the materials irrespective of the B site composition (Fe or Co or $\text{Fe}_{0.5}\text{Co}_{0.5}$) as is evident from Fig. 7a and b.

Charge density analyses for these surface terminations were conducted for interpretation of the stability trends. For

$\text{La}_{0.5}\text{Sr}_{0.5}\text{FeO}_3$, the stability of SrO surface termination over LaO termination was explained by the lower charge density of surface strontium ions ($0.163 \text{ e Bohr}^{-3}$) than that of lanthanum ions ($0.232 \text{ e Bohr}^{-3}$) on the surface of LaO termination. The charge density of the surface 'B' atoms and the oxygen atoms was similar for all the BO terminations. Hence, the stability among the BO terminations was better addressed by the inter-layer coulombic interactions. The surface charge density on the iron ions was calculated to be 0.48 e Bohr^{-3} , while that for lanthanum and strontium ions were $0.232 \text{ e Bohr}^{-3}$ and $0.163 \text{ e Bohr}^{-3}$, respectively. Fe_LaO termination has an iron-rich surface layer with lanthanum ions in the immediate sub-surface, while the sub-surface of Fe_SrO termination has strontium ions. Coulomb repulsion between the surface and sub surface layers being proportional to the product of the charge of the ions present on those surfaces, it is stronger between an iron-rich surface layer and a lanthanum-rich sub layer than that between an iron-rich surface layer and a strontium-rich sub layer. This accounts for more interlayer surface relaxation in Fe_SrO termination while less relaxation in Fe_LaO termination. This energy cost for more relaxation makes the Fe_SrO surface termination less preferred than Fe_LaO termination. The extent of relaxation in the top most surface is documented in Table 3.

Similarly, the different terminations that are formed along the (110) crystal facet are 'ABO' termination (having both the A site and B site components along with oxygen on the surface) and 'O' termination (having only oxygen on the surface lying atop the 'ABO' sub-surface). For $\text{La}_{0.5}\text{Sr}_{0.5}\text{BO}_3$, the only 'ABO' surface termination was $\text{La}_{0.5}\text{Sr}_{0.5}\text{BO}$ and the only 'O' layer is oxygen-atop- $\text{La}_{0.5}\text{Sr}_{0.5}\text{O}$ or simply $\text{O_La}_{0.5}\text{Sr}_{0.5}\text{BO}$. For $\text{La}_{0.75}\text{Sr}_{0.25}\text{BO}_3$, however, there are two types of 'ABO' terminations (LaBO and $\text{La}_{0.5}\text{Sr}_{0.5}\text{BO}$) based on the compositional variation of 'A' elements in the 'ABO' layer and hence the two 'O' terminated surfaces are O_LaBO and $\text{O_La}_{0.5}\text{Sr}_{0.5}\text{BO}$. The two terminations along the (110) planes of $\text{La}_{0.5}\text{Sr}_{0.5}\text{FeO}_3$ are shown in Fig. S4a and b† and the terminations along the (110) facets of $\text{La}_{0.75}\text{Sr}_{0.25}\text{FeO}_3$ are shown in Fig. S4c–f.†

The stability of the surface terminations along the (110) planes [Fig. 8a and b] was found to be dependent on the B site composition. In general, 'O' terminations were more stable than the 'ABO' terminations. For $\text{La}_{0.5}\text{Sr}_{0.5}\text{BO}_3$, the preference

**Fig. 8** Stability of the surface terminations along (110) crystal planes for (a) $\text{La}_{0.5}\text{Sr}_{0.5}\text{BO}_3$ and (b) $\text{La}_{0.75}\text{Sr}_{0.25}\text{BO}_3$ [B = Co, $\text{Fe}_{0.5}\text{Co}_{0.5}$ and Fe].

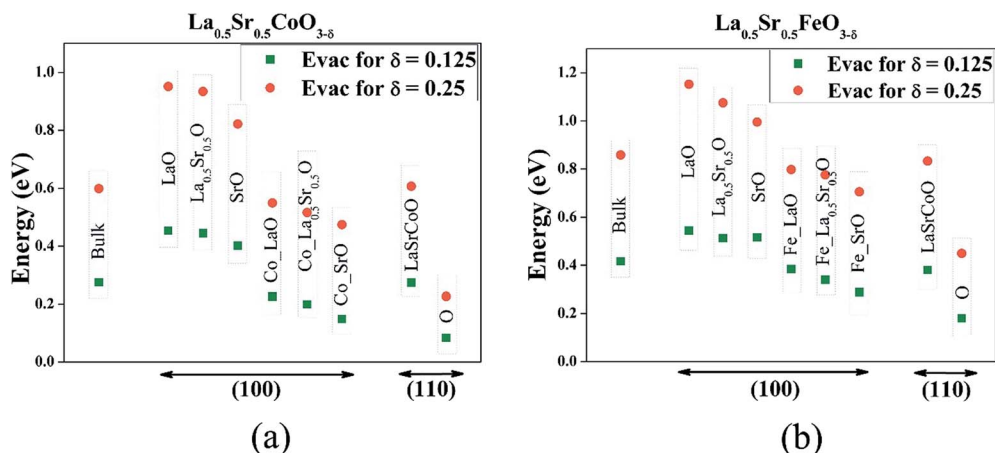


Fig. 9 Surface oxygen vacancy formation energy over various terminations along (100) and (110) for (a) $\text{La}_{0.5}\text{Sr}_{0.5}\text{CoO}_{3-\delta}$ and (b) $\text{La}_{0.5}\text{Sr}_{0.5}\text{FeO}_{3-\delta}$.

of 'O' termination becomes more pronounced with the increase of iron content in the B site. For $\text{La}_{0.5}\text{Sr}_{0.5}\text{CoO}_3$, the two terminations are almost equally stable. For $\text{La}_{0.75}\text{Sr}_{0.25}\text{BO}_3$, the most stable termination was O_LaBO, its preference increases with increased iron content in the 'B' site. For $\text{La}_{0.75}\text{Sr}_{0.25}\text{CoO}_3$, the O_LaCoO terminated surface exhibited almost similar stability to the $\text{La}_{0.5}\text{Sr}_{0.5}\text{CoO}$ terminated one. Between the two 'O' terminations, the stability was governed by the sub surface 'ABO' layer as is shown in Fig. 8b. Comparison amongst the absolute energies of the two sets of (100) and (110) surface terminations for all the six materials predicted easy formation of (100) crystal facets over (110). This surface termination stability is often not reflected in XRD patterns, as XRD is a bulk characterization technique.

These surface terminations are of particular interest as these are the most potent candidates to be generated under experimental conditions, both in stoichiometric and oxygen deficient states, and it is on these surfaces that the carbon dioxide conversion reactions occur.

4.4. Surface oxygen vacancies

Most of the catalytic reactions on oxygen deficient materials occur at or in the vicinity of the surface oxygen vacancy based active sites.^{61–66} Hence, a detailed investigation of the oxygen vacancies on the various surface terminations along (100) and (110) planes was conducted. The slab model for surfaces had 80 atoms. Hence, to create a vacancy of $\delta = 0.125$ and 0.25, two and four oxygen atoms were removed respectively from the surface. The oxygen vacancy formation was found to depend significantly on the local structure and composition of the surface. The surface oxygen vacancy formation trends across the various surface terminations were found to hold for all the materials, irrespective of the 'B' site composition. The oxygen vacancy trends on the different (100) and (110) surface terminations for $\text{La}_{0.5}\text{Sr}_{0.5}\text{CoO}_3$ and $\text{La}_{0.5}\text{Sr}_{0.5}\text{FeO}_3$ are reported in Fig. 9a and b, respectively, whereas the rest can be found in the ESI Fig. S5a–d.[†] The surface oxygen vacancy formation energies were different from the average bulk oxygen vacancy formation

energy. The energy to create $\delta = 0.125$ extent of oxygen vacancy in the bulk $\text{La}_{0.5}\text{Sr}_{0.5}\text{CoO}_3$ material was 0.275 eV per unit of ABO_3 , while that on the 'AO' terminated (100) surfaces was much higher (in the ranges of 0.40–0.45 eV/ ABO_3). The oxygen vacancy formation energies on the 'BO' terminated surfaces were less than the bulk values. The Co_SrO surface, in particular, was found to be really prone to accommodate the oxygen vacancies (vacancy formation energies found 0.125 eV lower than that of bulk). The (110) surfaces proved favorable towards oxygen vacancy generation as well. The oxygen-rich 'O'-terminations along (110) were the most favorable terminations for surface oxygen vacancy formation.

The same pattern was exhibited at higher concentrations of oxygen vacancy ($\delta = 0.25$) as well. For $\text{La}_{0.5}\text{Sr}_{0.5}\text{FeO}_3$ (Fig. 9b), and the other $\text{La}_{(1-x)}\text{Sr}_x\text{Fe}_{(1-y)}\text{Co}_y\text{O}_3$ materials, as in Fig. S5a–d,[†] the different surface terminations along (100) and (110) planes revealed a similar trend. Comparison amongst the oxygen vacancy formation energies in the bulk and across the 'AO' and

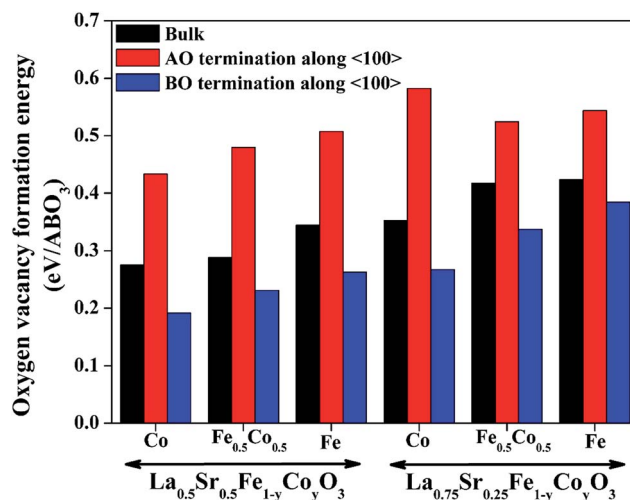


Fig. 10 Surface oxygen vacancy formation along 'AO' and 'BO' terminations of (100) planes of $\text{La}_{(1-x)}\text{Sr}_x\text{Fe}_{(1-y)}\text{Co}_y\text{O}_3$ [$\delta = 0.125$].

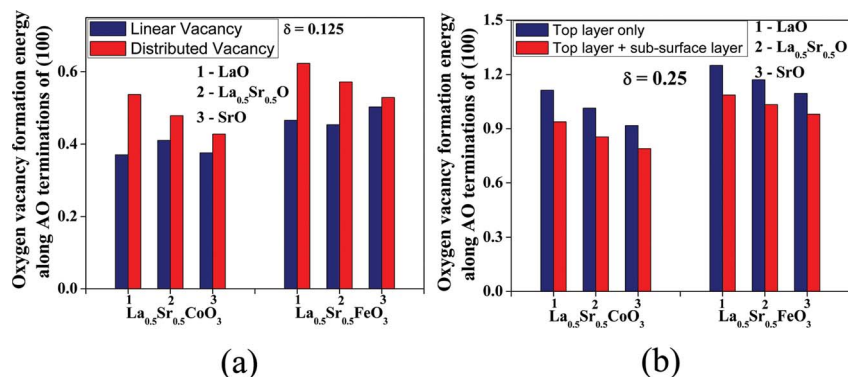


Fig. 11 Oxygen vacancy formation energies on different sites of AO surface terminations of $\text{La}_{0.5}\text{Sr}_{0.5}\text{BO}_3$ (a) linear and distributed vacancy sites for ($\delta = 0.125$) and (b) oxygen vacancy generation only on top surface and removal from both top and sub-surface.

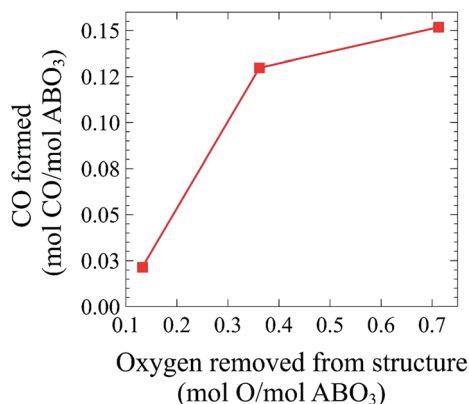


Fig. 12 CO formation as a function of oxygen removed from the $\text{La}_{0.5}\text{Sr}_{0.5}\text{FeO}_3$ surface during isothermal H_2 -reduction in the RWGS-CL process at 550 °C.

'BO' surface terminations for a vacancy extent of 0.125 is shown in Fig. 10. This trend of oxygen vacancy formation across various surface terminations was found to be valid for all the six materials. This provides a basis for surface selection for optimum oxygen vacancy formation. The site specificity of these vacancy formations was also revealed. Fig. 11a and b show the dependence of vacancy formation energy on the specific locations of AO terminated (100) surfaces. Oxygen vacancies along a linear chain was found favorable over a distributed vacancy formation (Fig. 11a). For a higher extent of oxygen vacancy formation ($\delta = 0.25$), a combination of sub-surface oxygen and surface oxygen removal was preferred over oxygen removal only from the top surface (Fig. 11b).

The surface oxygen vacancy creation also results in a significant amount of surface reconstruction, often exchanging oxygen between two consecutive layers. Certain surface terminations, particularly the 'BO' terminated surfaces [Fig. S7(a)†], were found to create trench like regimes on the surface after losing the surface oxygen. These crevices can serve as potential active sites for gas phase reactions (CO_2 reduction for thermochemical cycles).

4.5. CO_2 adsorption studies

The carbon dioxide adsorption energies on the perovskite surfaces are selected as descriptors for the CO_2 conversion reactions. The hypothesis is, stronger the adsorption, higher is the tendency of carbon dioxide reduction to carbon monoxide. The use of oxygen and hydrogen adsorption energies as suitable descriptors had been carried out in the past.^{33,34} Several studies on carbon dioxide adsorption on ceria and on metal surfaces have probed the best carbon dioxide adsorption configuration and the surface sites.^{67,68} The study here comprises only one of the adsorption states of carbon dioxide that has been compared over the different surface terminations of $\text{La}_{0.5}\text{Sr}_{0.5}\text{FeO}_3$ to reveal the role of oxygen vacancies and surface composition towards carbon dioxide conversion reactions. Although the trends of adsorption energies over the various surface terminations and vacancy concentration are assumed to hold for different adsorption configurations, studying the explicit effects of the CO_2 adsorption configurations on CO_2 adsorption strengths across different surface terminations is in progress. CO_2 conversion experiments revealed a strong dependence on oxygen vacancies as in Fig. 12 and computationally it has been performed by Daza *et al.* recently,¹³ thus establishing that

Table 4 CO_2 adsorption strengths across stoichiometric and oxygen vacant surface terminations of $\text{La}_{0.5}\text{Sr}_{0.5}\text{FeO}_3$

Surface oxygen vacancy extent	CO_2 adsorption energies on various surface terminations of $\text{La}_{0.5}\text{Sr}_{0.5}\text{FeO}_3$ (eV)			
	La_O termination	Sr_O termination	Fe_LaO termination	Fe_SrO termination
$\delta = 0$ [no vacancy]	−1.5135	−1.4822	−0.5736	−0.7800
$\delta = 0.125$	−3.8411	−1.9044	−0.7458	−1.1189

oxygen vacancy is the driving force for the CO₂ thermo-chemical conversion process.

The role of surface terminations was evident from Table 4; CO₂ adsorption strengths vary significantly across the different pure and non-stoichiometric surface terminations of La_{0.5}-Sr_{0.5}FeO₃. The adsorption strengths increase on oxygen vacant surfaces which is in accordance with the experimental results that state CO production rates increase with higher oxygen vacant surfaces as shown in Fig. 12. CO₂ was found to bind stronger on the 'AO' surface terminations in comparison to the 'BO' terminations. The adsorption strength was highest on the oxygen vacant La_O termination thus making it quite promising for CO₂ conversion to CO.

5. Summary and conclusions

A detailed investigation has been carried out on La_(1-x)Sr_xFe_(1-y)Co_yO_(3-δ) perovskite oxides. Computational studies *via* density functional theory has led to the proposition of probable crystal structure of the bulk materials. An increase of lattice constants for the cubic structures was noted for increased iron content in the 'B' site. The various surface terminations along (100) and (110) crystal facets of these materials were tested for stability; revealing a consistent trend of higher stability of the strontium-rich AO-terminated surface. This was true irrespective of the 'B' site composition. For the (110) surface terminations, the oxygen rich 'O' terminated planes were the natural choice for stability. The oxygen vacancy formation energetics both for the bulk systems and surface provided valuable insights. The trends of bulk oxygen vacancy formation energy were found to be in accordance with the experimental results, whereby increasing the iron content on the 'B' site led to a higher energy cost for oxygen removal, while the reverse pattern was true for increasing strontium content on the 'A' site. There was a consistent trend of easy bulk oxygen vacancy formation from the lanthanum-layers while it was more energy intensive from strontium-rich layers, mainly due to the easier redistribution for electronic cloud in the lanthanum-layers. Localized or tunnel-like oxygen vacancy formation was also found favorable in comparison to a more distributed vacancy generation. The stability of these materials at high oxygen vacancy concentration was revealed computationally and through *in situ* X-ray diffraction study of the La_{0.75}Sr_{0.25}-CoO₃ sample; thus making these materials a strong candidate for thermochemical reactions. On the other hand, the surface oxygen vacancy formation energy imparted valuable insights into the surface termination dependent oxygen vacancy generation. The 'BO' terminated (100) surfaces and (110) surfaces were favorable towards oxygen vacancy formation, while the 'AO' terminated (100) planes proved reluctant towards the same. There was also a strong dependence of surface oxygen vacancy formation energy on the various sites of surface terminations. The materials with different terminations were subsequently tested for carbon dioxide adsorption strengths as a descriptor for carbon dioxide conversion. Oxygen vacant 'AO' terminations along the (100) surface proved to be strong candidates for possible CO₂ conversion sites. In the perspective

of recent progress in preferential growth of surfaces of perovskites, this study paves the way for determining the desired surfaces for the energy intensive CO₂ conversion reactions.

Conflict of interest

The authors declare no competing financial interest.

Acknowledgements

The authors acknowledge NSF award CBET-1335817 and CHE-1531590 for financial support and USF Research Computing. DM acknowledges the Office of Graduate Studies, USF for the USF Graduate Fellowship. YAD acknowledges the USF School of Graduate Studies for the Graduate Student Success Fellowship, the Florida Education Fund for the McKnight Dissertation Fellowship and the NASA Florida Space Grant Consortium for the Dissertation Improvement Fellowship. The authors thank Ryan A. Kent for his help with synthesis of the samples.

References

- 1 G. Centi and S. Perathoner, *Catal. Today*, 2009, **148**, 191–205.
- 2 G. Centi, E. A. Quadrelli and S. Perathoner, *Energy Environ. Sci.*, 2013, **6**, 1711–1731.
- 3 D. Cheng, F. R. Negreiros, E. Aprà and A. Fortunelli, *ChemSusChem*, 2013, **6**, 944–965.
- 4 A. Steinfeld and R. Palumbo, *Encyclopedia of Physical Science & Technology*, 2001, **15**, 237–256.
- 5 T. Kodama and N. Gokon, *Chem. Rev.*, 2007, **107**, 4048–4077.
- 6 W. C. Chueh, C. Falter, M. Abbott, D. Scipio, P. Furler, S. M. Haile and A. Steinfeld, *Science*, 2010, **330**, 1797–1801.
- 7 J. R. Scheffe and A. Steinfeld, *Energy Fuels*, 2012, **26**, 1928–1936.
- 8 P. Furler, J. R. Scheffe, M. Gorbar, L. Moes, U. Vogt and A. Steinfeld, *Energy Fuels*, 2012, **26**, 7051–7059.
- 9 A. H. McDaniel, E. C. Miller, D. Arifin, A. Ambrosini, E. N. Coker, R. O'Hayre, W. C. Chueh and J. Tong, *Energy Environ. Sci.*, 2013, **6**, 2024–2028.
- 10 D. S. Mallapragada, N. R. Singh, V. Curteanu and R. Agrawal, *Ind. Eng. Chem. Res.*, 2013, **52**, 5136–5144.
- 11 J. R. Scheffe, D. Weibel and A. Steinfeld, *Energy Fuels*, 2013, **27**, 4250–4257.
- 12 Y. A. Daza, R. A. Kent, M. M. Yung and J. N. Kuhn, *Ind. Eng. Chem. Res.*, 2014, **53**, 5828–5837.
- 13 Y. A. Daza, D. Maiti, R. A. Kent, V. R. Bhethanabotla and J. N. Kuhn, *Catal. Today*, 2015, **258**(2), 691–698.
- 14 Q. Jiang, J. Tong, G. Zhou, Z. Jiang, Z. Li and C. Li, *Sol. Energy*, 2014, **103**, 425–437.
- 15 M. A. Peña and J. L. G. Fierro, *Chem. Rev.*, 2001, **101**, 1981–2017.
- 16 D. Klvana, J. Kirchnerová and C. Tofan, *Korean J. Chem. Eng.*, 1999, **16**, 470–4777.
- 17 M. Godickemeier, K. Sasaki, L. J. Gauckler and I. Reiss, *Solid State Ionics*, 1996, **86–88**(2), 691–701.
- 18 T. Ishihara, in *Perovskite Oxide for Solid Oxide Fuel Cells*, ed. T. Ishihara, Springer, US, 2009, DOI: 10.1007/978-0-387-77708-5_1, ch. 1, pp. 1–16.

- 19 J. Mizusaki, H. Tagawa, K. Naraya and T. Sasamoto, *Solid State Ionics*, 1991, **49**, 111–118.
- 20 A. Mineshige, J. Abe, M. Kobune, Y. Uchimoto and T. Yazawa, *Solid State Ionics*, 2006, **177**, 1803–1806.
- 21 A. H. Bork, M. Kubicek, M. Struzik and J. L. M. Rupp, *J. Mater. Chem. A*, 2015, **3**, 15546–15557.
- 22 A. M. Deml, V. Stevanović, C. L. Muhich, C. B. Musgrave and R. O'Hayre, *Energy Environ. Sci.*, 2014, **7**, 1996–2004.
- 23 A. M. Deml, V. Stevanović, A. M. Holder, M. Sanders, R. O'Hayre and C. B. Musgrave, *Chem. Mater.*, 2014, **26**, 6595–6602.
- 24 M. T. Curnan and J. R. Kitchin, *J. Phys. Chem. C*, 2014, **118**, 28776–28790.
- 25 X. Ma, B. Wang, E. Xhafa, K. Sun and E. Nikolla, *Chem. Commun.*, 2015, **51**, 137–140.
- 26 X. Ma, J. S. A. Carneiro, X.-K. Gu, H. Qin, H. Xin, K. Sun and E. Nikolla, *ACS Catal.*, 2015, **5**, 4013–4019.
- 27 C. Hou, W. Feng, L. Yuan, K. Huang and S. Feng, *CrystEngComm*, 2014, **16**, 2874–2877.
- 28 F. Sanchez, C. Ocal and J. Fontcuberta, *Chem. Soc. Rev.*, 2014, **43**, 2272–2285.
- 29 U. Treske, N. Heming, M. Knupfer, B. Büchner, A. Koitzsch, E. Di Gennaro, U. Scotti di Uccio, F. Miletto Granozio and S. Krause, *APL Mater.*, 2014, **2**, 012108.
- 30 Y. Orikasa, E. J. Crumlin, S. Sako, K. Amezawa, T. Uruga, M. D. Biegalski, H. M. Christen, Y. Uchimoto and Y. Shao-Horn, *ECS Electrochem. Lett.*, 2014, **3**, F23–F26.
- 31 Z. Feng, Y. Yacoby, M. J. Gadre, Y. L. Lee, W. T. Hong, H. Zhou, M. D. Biegalski, H. M. Christen, S. B. Adler, D. Morgan and Y. Shao-Horn, *J. Phys. Chem. Lett.*, 2014, **5**, 1027–1034.
- 32 J. Druce, H. Tellez, M. Burriel, M. D. Sharp, L. J. Fawcett, S. N. Cook, D. S. McPhail, T. Ishihara, H. H. Brongersma and J. A. Kilner, *Energy Environ. Sci.*, 2014, **7**, 3593–3599.
- 33 J. L. C. Fajín, M. N. D. S. Cordeiro, F. Illas and J. R. B. Gomes, *J. Catal.*, 2010, **276**, 92–100.
- 34 J. L. C. Fajín, M. N. D. S. Cordeiro, F. Illas and J. R. B. Gomes, *J. Catal.*, 2014, **313**, 24–33.
- 35 J. K. Norskov, T. Bligaard, J. Rossmeisl and C. H. Christensen, *Nat. Chem.*, 2009, **1**, 37–46.
- 36 P. Hohenberg and W. Kohn, *Phys. Rev.*, 1964, **136**, B864–B871.
- 37 W. Kohn and L. J. Sham, *Phys. Rev.*, 1965, **140**, A1133–A1138.
- 38 G. Kresse and J. Furthmüller, *Comput. Mater. Sci.*, 1996, **6**, 15–50.
- 39 G. Kresse and J. Hafner, *Phys. Rev. B: Condens. Matter Mater. Phys.*, 1993, **47**, 558–561.
- 40 G. Kresse and J. Furthmüller, *Phys. Rev. B: Condens. Matter Mater. Phys.*, 1996, **54**, 11169–11186.
- 41 P. E. Blöchl, *Phys. Rev. B: Condens. Matter Mater. Phys.*, 1994, **50**, 17953–17979.
- 42 G. Kresse and D. Joubert, *Phys. Rev. B: Condens. Matter Mater. Phys.*, 1999, **59**, 1758–1775.
- 43 J. P. Perdew and Y. Wang, *Phys. Rev. B: Condens. Matter Mater. Phys.*, 1992, **45**, 13244–13249.
- 44 L. Bengtsson, *Phys. Rev. B: Condens. Matter Mater. Phys.*, 1999, **59**, 12301–12304.
- 45 L. Wang, T. Maxisch and G. Ceder, *Phys. Rev. B: Condens. Matter Mater. Phys.*, 2006, **73**, 195107.
- 46 Y.-L. Lee, J. Kleis, J. Rossmeisl and D. Morgan, *Phys. Rev. B: Condens. Matter Mater. Phys.*, 2009, **80**, 224101.
- 47 G. Henkelman, A. Arnaldsson and H. Jónsson, *Comput. Mater. Sci.*, 2006, **36**, 354–360.
- 48 E. Sanville, S. D. Kenny, R. Smith and G. Henkelman, *J. Comput. Chem.*, 2007, **28**, 899–908.
- 49 W. Tang, E. Sanville and G. Henkelman, *J. Phys.: Condens. Matter*, 2009, **21**, 084204.
- 50 K. Momma and F. Izumi, *J. Appl. Crystallogr.*, 2011, **44**, 1272–1276.
- 51 Y. A. Daza, D. Maiti, B. J. Hare, V. R. Bhethanabotla and J. N. Kuhn, *Surf. Sci.*, 2016, **648**, 92–99.
- 52 S. A. T. Redfern, *J. Phys.: Condens. Matter*, 1996, **8**, 8267–8275.
- 53 S. Švarcová, K. Wiik, J. Tolchard, H. J. M. Bouwmeester and T. Grande, *Solid State Ionics*, 2008, **178**, 1787–1791.
- 54 B. P. Uberuaga and G. Pilania, *Chem. Mater.*, 2015, **27**, 5020–5026.
- 55 T. L. Nguyen, M. Dokiya, S. Wang, H. Tagawa and T. Hashimoto, *Solid State Ionics*, 2000, **130**, 229–241.
- 56 I. Kagomiya, K. Jimbo, K.-I. Kakimoto, M. Nakayama and O. Masson, *Phys. Chem. Chem. Phys.*, 2014, **16**, 10875–10882.
- 57 C. N. R. Rao and J. Gopalakrishnan, *New Directions in Solid State Chemistry*, Cambridge University Press, 1986.
- 58 T. R. S. Prasanna and A. Navrotsky, *J. Mater. Res.*, 1993, **8**, 1484–1486.
- 59 Y.-M. Kim, J. He, M. D. Biegalski, H. Ambaye, V. Lauter, H. M. Christen, S. T. Pantelides, S. J. Pennycook, S. V. Kalinin and A. Y. Borisevich, *Nat. Mater.*, 2012, **11**, 888–894.
- 60 J. N. Kuhn and U. S. Ozkan, *J. Catal.*, 2008, **253**, 200–211.
- 61 T. X. T. Sayle, S. C. Parker and C. R. A. Catlow, *Surf. Sci.*, 1994, **316**, 329–336.
- 62 G. Lu, A. Linsebigler and J. T. Yates, *J. Phys. Chem.*, 1995, **99**, 7626–7631.
- 63 M. A. Henderson, W. S. Epling, C. L. Perkins, C. H. F. Peden and U. Diebold, *J. Phys. Chem. B*, 1999, **103**, 5328–5337.
- 64 C. T. Campbell and C. H. F. Peden, *Science*, 2005, **309**, 713–714.
- 65 C. Yang, L.-L. Yin, F. Bebensee, M. Buchholz, H. Sezen, S. Heissler, J. Chen, A. Nefedov, H. Idriss, X.-Q. Gong and C. Wöll, *Phys. Chem. Chem. Phys.*, 2014, **16**, 24165–24168.
- 66 R. Schaub, P. Thosttrup, N. Lopez, E. Lægsgaard, I. Stensgaard, J. K. Nørskov and F. Besenbacher, *Phys. Rev. Lett.*, 2001, **87**, 266104.
- 67 Z. Cheng, B. J. Sherman and C. S. Lo, *J. Chem. Phys.*, 2013, **138**, 014702.
- 68 P. M. Albrecht, D.-E. Jiang and D. R. Mullins, *J. Phys. Chem. C*, 2014, **118**, 9042–9050.